Bone Fracture and Lesion Assessment using Shape-Adaptive Unfolding

H. Martinke[1,2], C. Petry[3], S. Großkopf[2], M. Suehling[2], G. Soza[2], B. Preim[1], and G. Mistelbauer[1]

[1] Otto-von-Guericke University, Magdeburg, Germany
[2] Siemens Healthineers, Forchheim, Germany
[3] ISO Software Systems GmbH, Nuremberg, Germany

The definite version of this article is available at https://diglib.eg.org:443/handle/10.2312/vcbm20171249

Citation:
Hannes Martinke, Christian Petry, Stefan Großkopf, Michael Suehling, Grezgorz Soza, Bernhard Preim, and Gabriel Mistelbauer: Bone Fracture and Lesion Assessment using Shape-Adaptive Unfolding. *In Proceedings of Eurographics Workshop on Visual Computing for Biology and Medicine* **2017**, pp. 149–158.

Eurographics Workshop on Visual Computing for Biology and Medicine (2017)
S. Bruckner, A. Hennemuth, and B. Kainz (Editors)

Bone Fracture and Lesion Assessment using Shape-Adaptive Unfolding

H. Martinke[1,2], C. Petry[3], S. Großkopf[2], M. Suehling[2], G. Soza[2], B. Preim[1], and G. Mistelbauer[1]

[1]Otto-von-Guericke University, Magdeburg, Germany
[2]Siemens Healthineers, Forchheim, Germany
[3]ISO Software Systems GmbH, Nuremberg, Germany

Abstract

The assessment of rib bone fractures and lesions consists of many images that have to be thoroughly inspected slice-by-slice and rib-by-rib. Existing visualization methods, such as curved planar reformation (CPR), reduce the number of images to inspect and, in turn, the time spent per case. However, this task remains time-consuming and exhausting. In this paper, we propose a novel rib unfolding strategy that considers the cross-sectional shape of each rib individually and independently. This leads to shape-adaptive slices through the ribs. By aggregating these slices into a single image, we support radiologists with a concise overview visualization of the entire rib cage for fracture and lesion assessment. We present results of our approach along different cases of rib and spinal fractures as well as lesions. To assess the applicability of our method, we separately evaluated the segmentation (with 954 data sets) and the visualization (with two clinical coaches).

CCS Concepts

•***Human-centered computing*** → ***Scientific visualization;*** •***Computing methodologies*** → ***Shape analysis;*** *Image processing;* •***Applied computing*** → ***Health informatics;***

1. Introduction

Traumatic as well as oncological chest pathologies often require a fast and precise assessment for treatment planning. As time is a crucial aspect to minimize negative impacts to the patient's health, suitable visualization techniques are required. For an examination, medical volume data is acquired, commonly computed tomography (CT) data sets for these particular cases. These data typically consist of thousands of axial sections or slice images, which have to be analyzed one-by-one, rib-by-rib and side-by-side. This is an exhausting and time-consuming task that has to be thoroughly performed by the referring physicians, since pathologies can be variable and inconspicuous if no dislocation is present or the fracture orientation is parallel to the section orientation.

To reduce the number of images to inspect, maximum intensity projection (MIP), a well-established visualization technique for medical examinations, projects 3D information on a single image. In CT data bone exhibits high intensity values, rendering MIP applicable to detect rib bone fractures within the cortical bone layer only. Fractures or lesions that leak into the spongy bone layer require to inspect the interior of the affected bone. Since ribs are tubularly shaped objects like blood vessels, similar techniques can be applied to them, such as curved planar reformation (CPR) (see Section 2) [KFW*02, KFWG06]. These methods cut along the centerline of a blood vessel to reveal its interior. To inspect the entire lumen of a vessel, these cuts can be rotated around its centerline. In a similar way, the Siemens syngo.via CT bone reading (sCTBR) technique enables radiologists to inspect ribs through straightened planar cuts, leading to a proper assessment of bone fractures and lesions (see Section 3) . However, this approach still requires a substantial degree of interaction, making the analysis of pathologies a time-consuming process.

Visualizing the entire rib cage in a single image would simplify and accelerate the diagnosis of bone pathologies. In this work, we present a prototype (see Section 4), which visualizes the entire rib cage unfolded and aggregated into a single image. Concisely, our contributions are:

- A segmentation of the ribs and vertebrae, including the separation of the cortical (hard bone) and spongy (soft tissue) layers,
- Two unfolding approaches: radial and shape-adaptive,
- A slab rendering projection technique for dimensionality reduction and highlighting of different rib and spinal pathologies, and
- A standardized and obstruction-free anatomical layout.

We implemented our prototype in the Siemens syngo.via frontier application framework (see Section 5) and show several cases of rib/spinal fractures and lesions (see Section 6). We evaluated the stability and accuracy of our unfolding approach (see Section 7) and conclude our work with future remarks (see Section 8).

2. Related Work

The technique proposed in this work combines several aspects of MIP, CPR and curvicircular feature aggregation (CFA). The goal is to provide an overview of the entire rib cage or the spine to support clinicians during the assessment of bone fractures and lesions.

Curved planar reformation. Commonly, volumetric medical data are explored using planar cuts. Most widespread are axis-aligned slice views, such as the axial, coronal or sagittal slices. Since they present the data unchanged to the physician, they are an integral part of medical reporting and visual assessment. Nevertheless, their inspection is a time-consuming process that can be accelerated for specific anatomical structures, e.g., blood vessels or bones. To inspect the interior of a single blood vessel, curved planar reformation (CPR) has been introduced [AMRB98, KFW*02, AMB*13] with its extension to multiple blood vessels, referred to as multi-path curved planar reformation (mpCPR) [KFW*02, KFWG06]. By creating a curved cut along a vessel's centerline, the lumen of a blood vessel is revealed without any obstruction. In order to review the entire blood vessel for potential stenoses, the lumen has to be inspected from all viewing directions, i.e., the CPR has to be rotated around the centerline – increasing the number of images to inspect. Curvicircular feature aggregation (CFA) addresses this aspect by casting circular rays, starting from the centerline point, outwards, and applying different projection techniques, such as MIP or minimum intensity projection (MinIP) [MMV*13]. This captures the whole lumen of a blood vessel within a single image. In case of CT angiography data, the former projection depicts calcification and the latter soft plaque, both indicators for stenotic regions. However, CFA assumes that vessels mainly exhibit circular cross-sections. Motivated by their method, we extend it to arbitrary cross-sectional shapes and different application scenarios, such as rib fractures and spinal lesions.

Unfolding. In order to provide an obstruction-free view of relevant 3D anatomical structures (e.g., skull [RSS*10], ribs [RLT*15], heart [TBB*07], placenta [MMK*17]), they have to be unfolded. If such a 2D view is further standardized, inter-patient comparison is favored. Kretschmer et al. [KST*14] consider the entire shape of an object for their anatomy-driven reformation (ADR). To reduce distortions during an as-rigid-as-possible transformation and support objects of different shapes, they use the harmonic triangulation by Floater [Flo97]. Marino and Kaufmann [MK16] describe an approach thats flattens the surface of vascular structures without self-intersections and obstructions. Kaftan et al. [KKW*14] use virtually straightened CPRs for rib fracture assessment. By rotating around each rib's centerline, which has been detected using deformable template matching [WLP*12], a fracture can be quickly spotted. To retain the spatial context, they arrange the ribs in an anatomical layout, with the spine in the center. Despite reducing information to several CPR images, their number is still large for all the ribs. Motivated by this fact, our technique overcomes this problem by proposing a single image for rib fracture assessment. Termeer et al. [TBB*07] present a standardized representation of the myocardium, called *volumetric Bull's eye plot*. It allows physicians to assess the distribution of scar tissues, although the structure of the myocardium might locally vary across different patients. The myocardium is unfolded into a cylinder such that samples of a particular slice, which exhibit a certain distance to the epicardium and endocardium, are arranged into a circle. Miao et al. [MMK*17] describe a technique for unfolding the surface of the human placenta in utero into two sides: the maternal and fetal sides. Both are represented as circles in order to mimick the conventional ex vivo inspection of the placenta. Ringl et al. [RSS*10] unfold the human skull to quickly spot skull fractures using a curved MIP. Saroul [Sar06] investigated geometrical properties of 3D surfaces projected into 2D space, such as distortions. It is essential for physicians to know the amount of the introduced distortions, e.g., for distance measurements on flattened surfaces. As we map the ribs to a rectangular region of fixed height, the distortion increases the farther we slice into the ribs.

Anatomical layouts. With increased abstraction of a visualization, the spatial context usually deteriorates. To counteract this problem, several layouts for different anatomical regions have been proposed. Borkin et al. [BGP*11] describe a layout for vascular structures. By unfolding and straightening the surface of the coronary arteries and simultaneously encoding the endothelial shear stress, a concise overview of the vascular system is provided. However, this layout can be quite elongated, depending on the length of the blood vessels. For the investigation of peripheral arterial occlusive diseases of the human lower extremities, Mistelbauer et al. [MMV*13] propose a layout with the aorta being in the center and extending left and right according to the respective branch. Sorger et al. [SBS*13] introduce a layout for assessing the neural circuit of a fruit fly alongside an abstract view of the underlying brain.

3. Medical Background

Bone fractures and oncological lesions are most common pathologies in the human thorax. A correct diagnosis of these diseases is important to implement the necessary treatment.

Rib bone **fractures** often occur after a blunt thoracic trauma and immediate care is required, also due to possibly damaged surrounding inner organs [ZA94, KMU*12]. The distribution of the fracture and number of broken ribs influence the posttraumatic complications and the mortality [BHL*14]. Hence, it is of medical relevance to correctly detect rib pathologies in a time-efficient manner and to implement the proper treatment [BSO*15]. Schulze et al. [SHS*13] distinguish between different types of fractures, depending on which cortical bone lines are affected (see Figure 1). When both cortical lines are interrupted, it is referred to as *complete fracture*. A *partial fracture* is described by only one interrupted line and referred to as inner and outer cortical fracture, respectively. If the interrupted line is pinched, it is referred to as *buckle fracture* [YLO11].

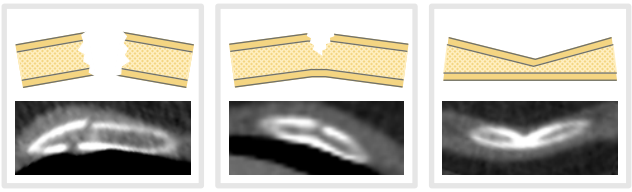

(a) Complete (b) Partial (c) Buckle

Figure 1: *Different types of rib bone fractures. (a) shows a complete fracture, (b) a partial fracture, and (c) a buckle fracture.*

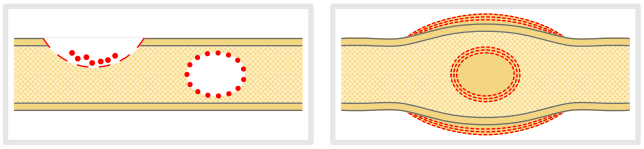

(a) Osteolytic (b) Osteoblastic

Figure 2: *Two different types of bone lesions. (a) shows osteolytic lesions that successively destroy the bony tissue. These lesions can be located in both bone layers (cortical & spongy). (b) demonstrates the behavior of an osteoblastic lesion. It starts inside the bone and grows bony tissue until the bone breaks due to the increased stress induced by the lesion.*

Oncological **lesions** in the ribs or vertebrae are usually spread metastases of a cancer. These metastases can occur in bones as osteolytic (bone resorbing) or osteoblastic (bone forming) lesions [OL12, KW15]. **Osteolytic metastases** (see Figure 2a) are with 75% the most common bone metastases in the human thorax. These lesions stimulate directly or indirectly the osteoclastic activity, resulting in bone resorption [GMC*06]. In their early formation phase, the bone membrane degrades. Consequently, tumor cells produce hormones that stimulate the osteoclasts, continuing bone resorption. This endangers the stability of the whole human thorax, a potentially lethal development for a patient. **Osteoblastic metastases** (see Figure 2b) are usually present in prostate cancer [MS11]. This cancer metastasizes to the rib cage and locally remodels the normal bone structure. This process is unordered and has an unstructured micro-architecture, leading to a reduced bone stability, which increases the risk of fractures and potential lethal injuries of inner organs [GMC*06]. Consequently, an accurate detection of the tumor stage significantly impacts the prognosis and decision of the proper therapeutic method [HMD*15].

4. Methodology

In order to aid physicians during bone fracture and lesion assessment, we propose a standardized visualization of the entire rib cage and spine. The workflow of our procedure (see Figure 3) consists of the following four steps: segmentation, smoothing, unfolding and visual mapping. Firstly, the ribs or vertebrae are segmented and separated into their cortical and spongy bone layers. In the second step, these segmented parts are smoothed by a novel resampling strategy. Thirdly, each rib or vertebra is unfolded and, in the final and fourth step, combined into a standardized visualization by using common projection techniques to highlight potential pathologies.

Our approach requires the centerlines of either the ribs or the spine as input. These 3D curves are then equidistantly sampled – following the Nyquist-Shannon theorem – to compute the local coordinate frame at each of these 3D spatial positions. Additionally, the bounding boxes of the vertebrae are retrieved from the sCTBR module of the software framework where our technique has been implemented. All ribs and vertebrae are annotated with their correct anatomical position.

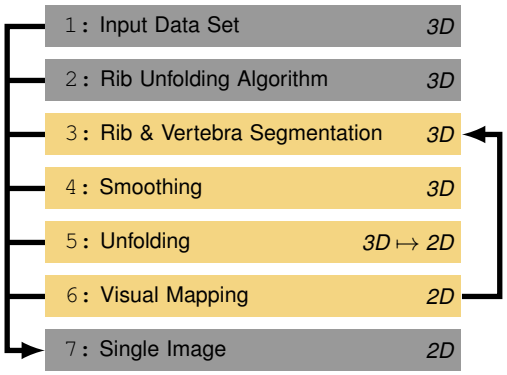

Figure 3: *Our workflow for bone fracture and lesion assessment. Having an input data set loaded, the subsequent rib unfolding algorithm [RLT*15] provides the required centerlines and coordinate frames. After segmenting the ribs and vertebrae, specifically their cortical and spongy bone layers, their segmentation is smoothed and unfolded. By visually mapping them to an anatomical layout, we retain spatial context.*

4.1. Rib & Spine Segmentation

Bones typically consist of two layers, the hard (cortical) and soft (spongy) tissue. Certain pathologies affect only one layer, such as oncological lesions. If we would not distinguish between the two bone layers, these pathologies could be missed during an examination. To avoid such diagnostic errors, physicians usually check up with slice views, which is again a time-consuming task. Our approach accounts for this by segmenting both bone layers.

Before we start segmenting the cortical bone layer, we define the region-of-interest to fit only the ribs and spine, neglecting the other parts of the input thoracic volumetric data set. We further divide the ribs into outward (anterior) and inward (posterior) parts. The former ones contain the ribs only, whereas the latter ones include the vertebrae and the origins of the ribs. These two parts are separated by the bounding box around the vertebrae to prevent the rib segmentation algorithm from leaking into the spine. However, the same phenomenon occasionally occurs for the sternum. We solve this problem by extruding the bounding box anterior to the extent of the data set to definitely include the sternum.

We employ 3D region growing using 6-connectivity, which performed best throughout all our conducted experiments, for segmenting the **cortical rib bone layer**. Starting with the outward part, we use the equidistantly sampled points along the rib centerlines as seed points, but locally shift them upwards and downwards along their respective upvectors, starting from the centerline point. The length of the shift is limited by half the maximum rib thickness (38 voxels throughout all our examples and results), which guarantees at least one contact point with the cortical bone. Since certain pathologies, such as osteoblastic lesions, exhibit a similar intensity range – Hounsfield units (HU) in our case – we have to specify the threshold value for the inclusion criterion of the region growing rather strict, e.g., a lower threshold value of 400 HU that only describes the cortical bone. For the inward parts of the ribs, we use region growing again. However, in this case, it leaks into the verte-

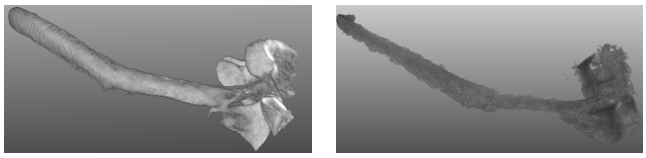

(a) Cortical bone (b) Spongy bone

Figure 4: *Segmentation of the cortical and spongy rib bone layers.*

brae. Model-based segmentation techniques might be more suitable for this task. The inward and outward parts are then connected using a logical *or* operation (see Figure 4a).

The separation of the **spongy rib bone layer** from the cortical one is achieved by a morphological closing operation of the cortical bone. This closes the entire cortical bone region as well as the open connection with the sternum. We chose a spherical structuring element of radius 11 voxels to ensure completely enclosing the cortical bone. In order to separate the spongy bone now, the closed image will be masked with the segmentation mask of the cortical layer using a logical *xor* operation. This results in a binary mask of the spongy and the cortical bone layers. To obtain the original intensity values, this binary mask is used to access the input data set (see Figure 4b).

For segmenting the vertebrae of the **spine**, we employ a method similar to the rib segmentation. To avoid oversegmentation, we limit the region growing to a bounding box that contains the entire vertebra that we want to segment. The seed points for the segmentation are obtained from the centerline that goes through the body of the vertebra. For segmenting the cortical bone layer of the vertebra, we use the same threshold value as for the ribs. However, a separation of the cortical and spongy bone is not possible due to the noise and limited contrast of the CT data. The reason for this could be the anatomical function of the osteoclasts in the spine. They create a formation of cortical bone structures, represented as branches of cortical bone in the direction to the cortical bone layer [May16]. Consequently, we use a morphological closing operation to segment the complete vertebra.

4.2. Smoothing

The segmentation of the cortical and spongy rib bone layers exhibits strong *terrace artifacts* (see Figure 5a). They originate in the reconstruction algorithm of the raw CT data [Her09], as it is limited by the pixel matrix of the output image (commonly 512×512 or 1024×1024). Another source is the angle between the normal vector of the axial slice plane and the rib direction. The larger this angle, the stronger pronounced are these artifacts [BHP06].

As these artifacts affect the subsequent unfolding algorithm (see Figure 3), we address this problem by upsampling the segmented structures. We compute the intensity values at the new voxel locations using cubic interpolation of existing voxels (see Figure 5b). Alternatively, linear or Lancosz interpolation could be used, but they result either in decreased accuracy or in longer computing times. After analyzing several data sets, we empirically chose a scale factor of three along all axes for upsampling.

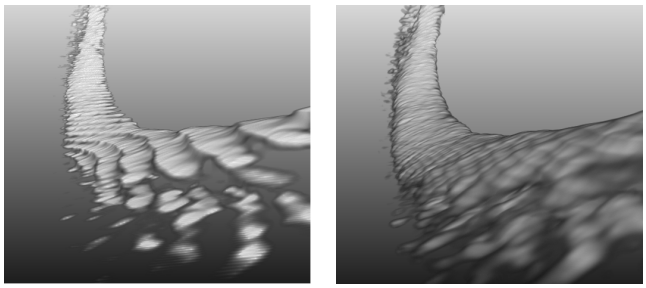

(a) Original (b) Upsampled

Figure 5: *Comparison between the normal rib voxel structure (a) and the upsampled image (b).*

4.3. Unfolding

After segmenting the cortical and spongy bone layers of the ribs, they have to be unfolded in order to provide physicians with a suitable overview image for their diagnosis. To assess a bone fracture or lesion, the entire structure of the bone has to be captured for visual analysis of either the cortical layer or the spongy layer, or even both simultaneously. Ringl et al. [RLT*15] chose a CPR for rotating around the ribs' centerlines to assess the entire bone structure. As this results in a lot of images to analyze, we aim to reduce them to only a single one. This further removes any required interaction and offers a standardized view of the patient's rib bones for fracture or lesion diagnosis. As the subsequent unfolding can be analogously applied to the vertebrae without any adaptations, we only describe it on the basis of the ribs.

Motivated by Mistelbauer et al. [MMV*13] for radially sampling a tubular structure, we create **radial slices** in cross-sections perpendicular to the centerline, starting from the centerline outwards (see Figure 6a). Instead of aggregating these radial slices into a single value, we unfold them to a specific length. This length can be specified by the user and is constant across all ribs. The concentric radial slices are propagated until their diameter exceeds a maximum extent (38 voxels, around 2–3 cm for different voxel resolutions), which we estimated across 300 data sets. This should ensure that the entire bone is captured, as it is preferred to capture more than not enough. Once unfolded, we get a 3D stack of 2D slice images. Their combination into a single image is described in Subsection 4.4. However, radial slices do not adapt to the elliptical shape of the rib bones, resulting in empty regions when leaving the ribs, especially with increasing radii. These regions appear dark due to the lower intensity values of the tissue surrounding the ribs, leading to a severe deterioration of the visualization, as demonstrated in Figure 6a along the images with $z = 4$ and $z = 5$.

We tackled this problem with **shape-adaptive slices**. In contrast to the structure-aware slicing proposed by Miao et al. [MMK*17], we do not employ a distance field for computing the slice, but rather a ray-casting approach. Since the ribs are segmented, their cross-sectional shape is known. By shooting rays – originating at the centerline – outwards, each ray measures the length until it leaves the cortical bone layer of its corresponding rib. This length is then subdivided by a user-specified number of samples (z-axis), for each ray independently. This leads to a sparser sampling of

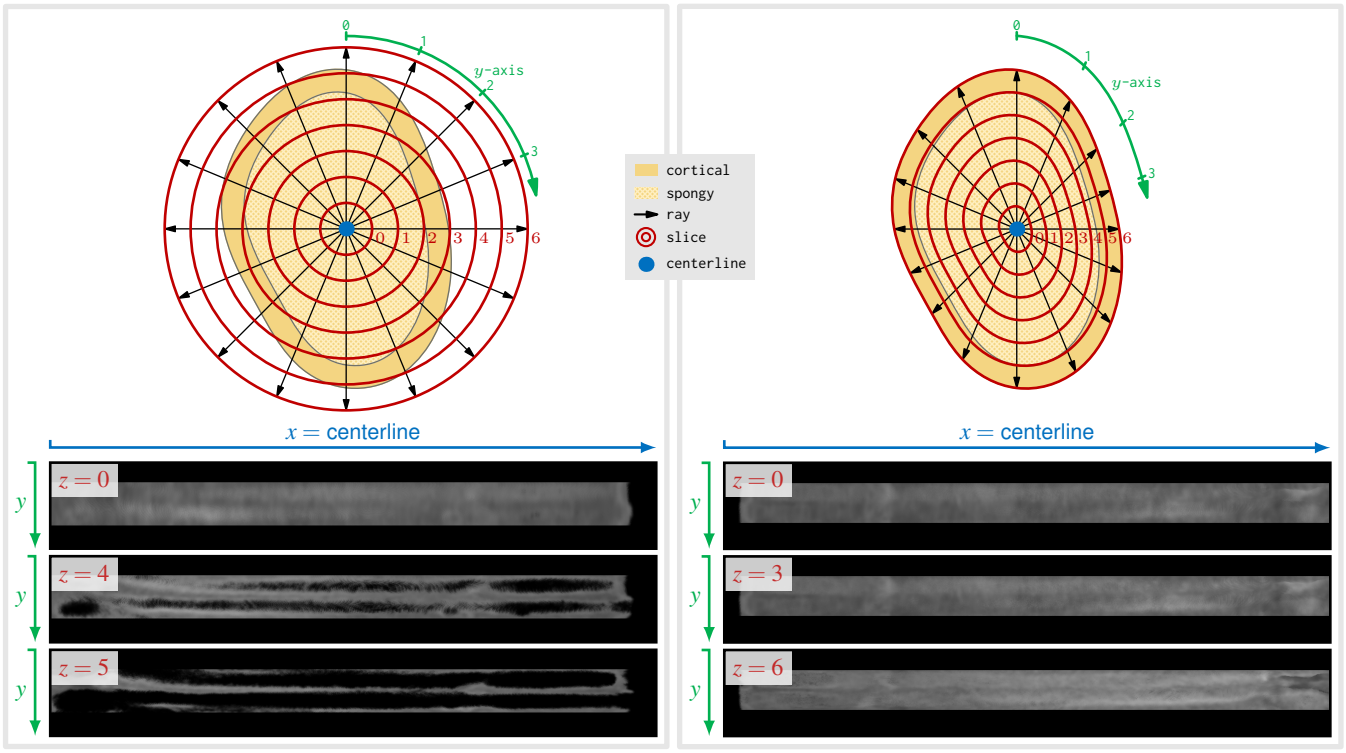

(a) Radial (b) Shape-adaptive

Figure 6: *Comparison between our two different unfolding approaches. (a) shows concentric radial slices starting from the centerline, progressing outwards. At a certain radius, the slices leave the ribs in some regions, reflected by alternating dark areas in the image ($z = 5$). (b) presents the shape-adaptive slices. By computing independently for each ray the position when it leaves the cortical bone, the distances of consecutive samples are different between rays. The resulting slices adapt to the shape of the rib bones and do not exhibit any artifacts.*

longer rays and a denser sampling of shorter ones. Samples with the same indices across all rays are then connected to form the shape-adaptive slices (see Figure 6b). Each of these slices is subsequently unfolded to a rectangle of fixed height (= number of rays, y-axis), again leading to a 3D stack of 2D slice images. As this approach approximates the shape of the ribs well, it provides an artifact-free visualization even of slices at the boundary of the ribs.

4.4. Visual Mapping

Once we have unfolded all slices of the ribs or spine, we obtain several 3D stacks of 2D slices. To reduce and simplify the interaction, we propose two approaches. Firstly, we reduce the number of slices to a single image using projection techniques such as MIP or MinIP. Secondly, these resulting images are arranged in a standardized anatomical layout that reflects the anatomy of the relevant object of interest (see Figure 7). Both aspects are subsequently explained.

For every slice of each rib/vertebra (see Figure 6) we retrieve a rectangle, where the length of the rib/vertebra or its centerline is mapped to the width (x-axis) and the number of rays to the height (y-axis). Since all ribs/vertebrae have the same number of shape-adaptive slices (z-axis), we employ a slab rendering using different projection methods, each with its own important aspects relevant for diagnosis. This reduces the number of images to inspect from several shape-adaptive slices to a single image per rib or vertebra, avoiding slicing through the entire 3D image stack [PB14]. When using MIP (see Figure 9b) in conjunction with the cortical bone layer only, one can clearly identify complete and partial fractures, but not lesions. The latter are revealed when using the spongy bone layer, either with MIP for osteoblastic lesions or with MinIP for osteolytic lesions.

Dislocated complete rib bone fractures potentially lead to improperly defined centerlines, causing the CPRs of the ribs to overlap in the conventional visualization (see Figure 8a). To avoid this problem, we decided for a fixed layout of the unfolded rib visualizations, while retaining the anatomy of the entire rib cage as spatial context (see Figure 8b). The ribs are arranged on the left (patient right) and right (patient left) side of the image respectively, resembling a vertical layout (see Figure 7a). This results in a standardized visualization, where every unfolded and aggregated rib has its fixed position, even across patients. By associating a unique index with each unfolded rib bone, the 3D position of the cursor can be determined to link the visualization with a conventional slice view. This view offers a general reading protocol of the image.

The layout of the spine is implemented by individually unfolding each vertebra and horizontally arranging them within the final image (see Figure 7b). The vertebrae are ordered with the anatomical superior on the left side and the anatomical inferior on the right side.

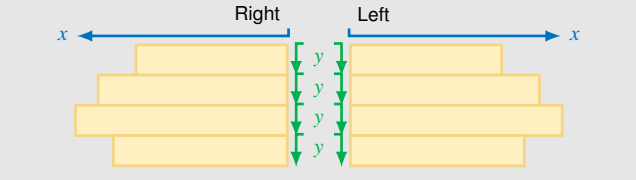

(a) Ribs

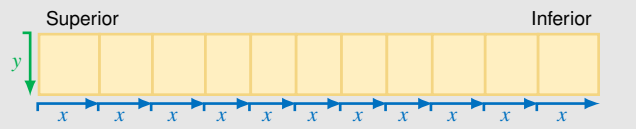

(b) Vertebrae

Figure 7: *Visual mapping of ribs and vertebrae to a standardized layout. (a) presents the anatomical layout of the ribs. Every rib is independently unfolded to a fixed height (y-axis, number of rays) and variable width (x-axis, centerline length) and placed at its corresponding anatomical position. (b) shows the layout of the vertebrae. Analogously to the ribs, each vertebra is unfolded, but placed from left (superior) to right (inferior).*

5. Implementation

Our visualization approach is integrated in the Siemens *syngo.via Frontier Development Kit*. This includes the standard MeVisLab development environment [RBH*11] with extended components of the *syngo.via Frontier application framework*. By using this framework, our prototype resembles a common medical application with the standard user interface design and components, including a development documentation. This prototype can be uploaded to the Frontier server, which is the research data base. Furthermore, a connection between the research platform and the clinical workflow allows clinical partners to immediately evaluate such prototypes. Their feedback can then be incorporated into an improved version of the prototype. All frontier prototypes are only allowed for research purposes and not for the clinical routine [Sie16].

6. Results and Discussion

In this section, five cases are presented. The first two cases represent different types of rib bone fractures, whereas the following case shows an oncological lesion visualized by our rib unfolding algorithm. The remaining two cases demonstrate how our visualization performs for spinal fractures and metastases. Eventually, we discuss limitations of our visualization technique.

Rib bone fractures are presented in Figure 8 and Figure 9. A case with multiple complete rib fractures (highlighted with red circles) is presented in Figure 8. All fractures are complete, discernible due to their darker vertical intensity value variations throughout their respective entire rib and well perceivable in both MIP (see Figure 8b) and MinIP (see Figure 8c). Figure 9 shows a case with different partial and buckle fractures (highlighted with red circles). They can be discerned by a partially dark vertical intensity value variation, which does not stretch along the entire height of the unfolded rib. Since fractures are again investigated, some might be missed when solely inspecting a MIP of the cortical and spongy layer together. As demonstrated in Figure 9b with a MIP of the cortical layer only, two more fractures are revealed.

Osteoblastic **rib bone lesions** are demonstrated in Figure 10. They manifest as bright spots within the unfolded rib visualization. As the cortical rib bone layer exhibits rather high intensity values, the contrast between the lesions and the bone background deteriorates (see Figure 10a). It is therefore recommended to exclude the cortical bone and utilize the spongy layer solely. As presented in Figure 10b, the lesions are more prominently visible. To distinguish between the two types of lesions (recall Section 3), different projection methods can be used. The bright osteoblastic lesions are well captured by a MIP. The bone absorbing osteolytic lesions usually occur as dark regions in the unfolded image. Consequently, they are well highlighted by a MinIP.

Spinal fractures are well depicted within our unfolded anatomical layout, as shown in Figure 11a (highlighted with red circles). They manifest as deformed dark regions in our unfolded visualization. Osteoblastic and osteolytic **spinal lesions** are presented in Figure 11b. Analogously to rib bone lesions, the bright ostoblastic or the dark osteolytic regions can be highlighted with MIP and MinIP, respectively.

Our visualization approach has some **limitations**, which are discussed in the following. The segmentation of the inward rib part can be improved, as it currently leaks into the spine. A more precise segmentation would also improve the extraction of the centerlines, as they are prerequisites of our approach and we currently rely on the sCTBR for extracting them. In case the centerline or the required bounding box around the vertebrae is not properly determined or even missing, some parts of the bone cannot be segmented or unfolded and remain empty in our visualization. Our shape-adaptive slicing currently handles only convex shapes; concave ones have to be handled with care. One could initially compute a distance field and then adapt the distances to the boundary to the desired number of slices. Furthermore, a medial surface might be considered instead of a medial axis or centerline. However, we did not encounter any concave cross-sectional shapes in all our tested data sets, neither in the ribs nor in the vertebrae.

7. Evaluation

In order to assess the applicability of our approach, we separately evaluated the segmentation and unfolding. We tested our segmentation with a large number of data sets and consulted clinical coaches for the unfolding. Subsequently, we explain the outcome of both.

To evaluate the reliability of our **segmentation** algorithm, we conducted a quantitative comparison of 954 data sets. These data were acquired with different CT scanners, scanning parameters, and reconstruction kernels, in order to respresent the wide variety that occurs in clinical practice. Consequently, an independent test series is warranted, since the slice thickness has been additionally varied between 0.5 mm and 5 mm. As a ground truth segmentation has not been readily available, our evaluation provides an informal assessment of the stability and confidence of our algorithm. In consideration of the given data sets, 872 (91.4%) could be properly segmented and unfolded. In 60 data sets (6.3%) some ribs remained missing, due to improperly segmented centerlines of the sCTBR.

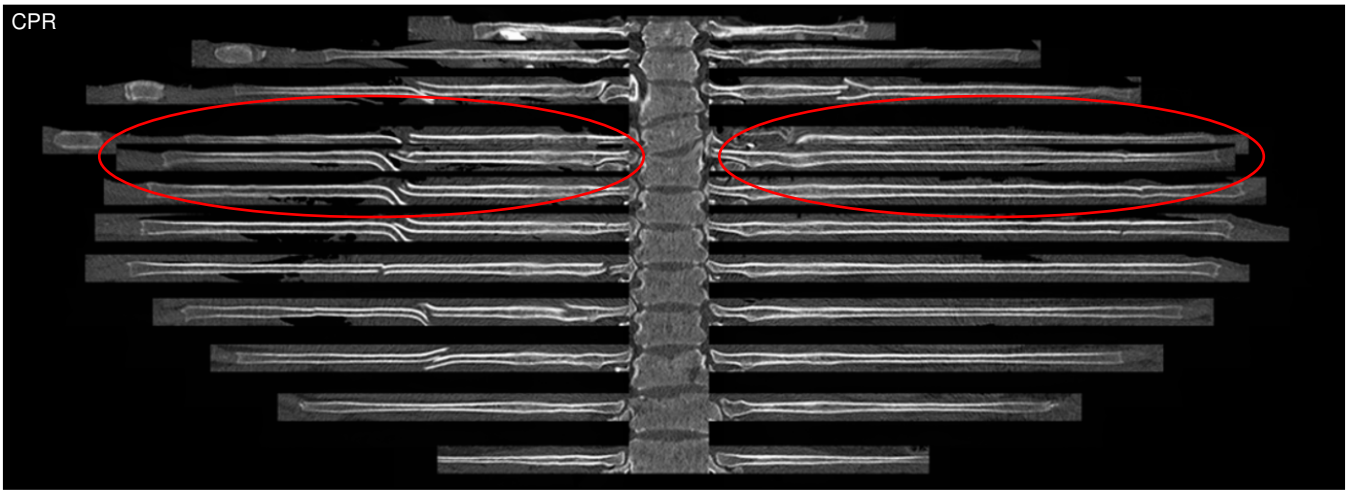

(a) Conventional layout

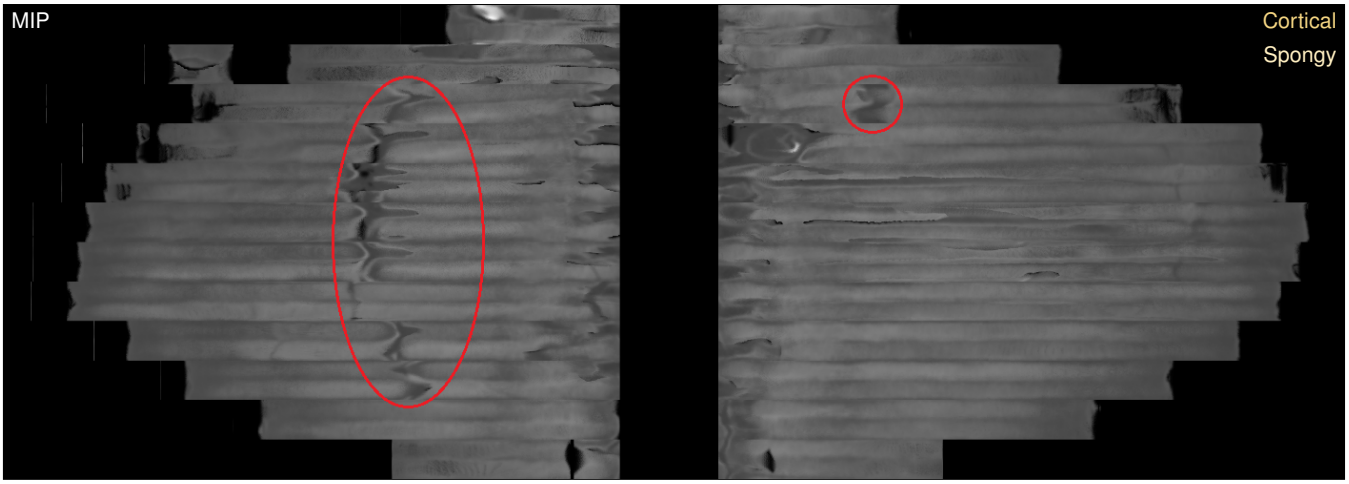

(b) Anatomical layout

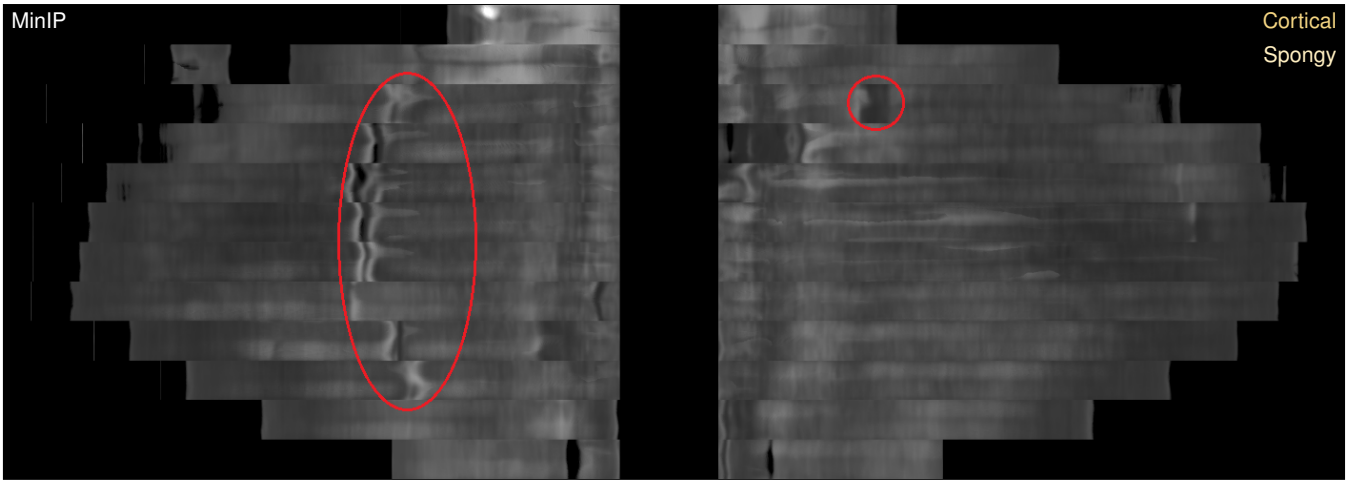

(c) Anatomical layout

Figure 8: *Case with multiple complete rib bone fractures. (a) shows the conventional layout using CPRs of the sCTBR for assessing rib fractures. Since the ribs are not unfolded to a fixed height, several ribs are overlapping (red circles), hindering the assessment. Our fixed anatomical layout is presented in (b) using a MIP of both bone layers (cortical & spongy), whereas (c) displays a MinIP. All broken ribs (red circles) are depicted with neither artifacts nor obstruction in our visualizations.*

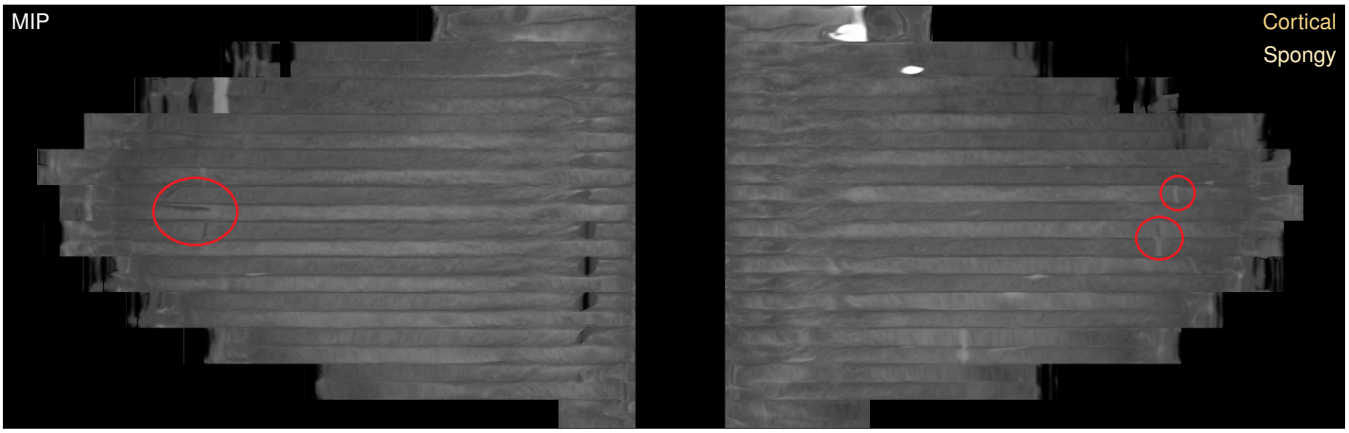

(a)

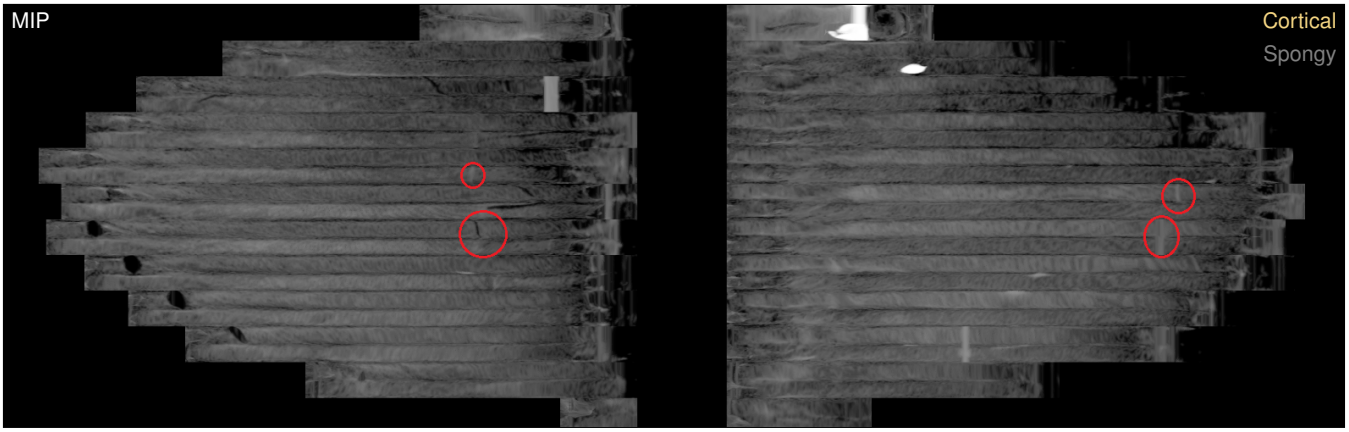

(b)

Figure 9: *Case with partial and buckle rib bone fractures. (a) shows multiple partial and buckle rib bone fractures using a MIP of both bone layers (cortical & spongy). Since (b) presents a MIP that only uses the cortical bone layer, two more partial fractures are revealed. This clearly demonstrates the advantage of having the possibility to inspect both bone layers together or separately.*

In 22 data sets (2.3%) our algorithm did not achieve satisfactory results, but the sCTBR did not deliver the required input beforehand. The segmentation duration depends on the size of the tested data set and is one minute on average.

We qualitatively evaluated our **unfolding and visual mapping** by consulting two clinical coaches of Siemens Healthineers, who are specialized in trauma and oncological diagnostic tasks. These clinical coaches bridge the algorithmic prototype development with the clinical partners. They define the clinical tasks and requirements and focus on the appropriate execution of the functionality and algorithm. These coaches tested our prototype for around one hour with different data sets and compared their visual experiences with the sCTBR. Both reported that our proposed visualization exhibits the following benefits over the sCTBR: *(I)* Our approach could save time for diagnosing fractures and lesions, and *(II)* regarding the clinical workflow with our method, they were particularly confident that only a few interaction steps are necessary to examine bones more accurately. However, both coaches stated that an initial accomodation time is required to get familiar with our prototype. They only critized the possible intrinsic image artifacts that could be misinterpreted as pathologies, but this can be interactively verified on the original CT slices. Most of these artifacts might be reduced by improving the sCTBR agorithm.

8. Conclusions and Future Work

We presented a novel visualization approach that unfolds objects in a shape-adaptive manner. By considering the cross-sectional shape of the ribs or vertebrae, we provide a single image for bone fracture as well as lesion assessment. This approach reduces the required amount of images to inspect, and accelerates the entire assessment process. To this end, we support physicians with a fixed anatomical layout of the unfolded ribs. As this layout is standardized, pathological cases can be compared even across patients.

In future work, we would like to improve both aspects, the segmentation and visualization. Multiscale vessel enhancement filters could be applied to the ribs as well, since they exhibit a similar tubular shape-like structure. The visualization could be improved by providing annotations of the respective ribs or vertebrae together with their pathologies. Such a visualization could also be used as an overview map for a diagnostic report.

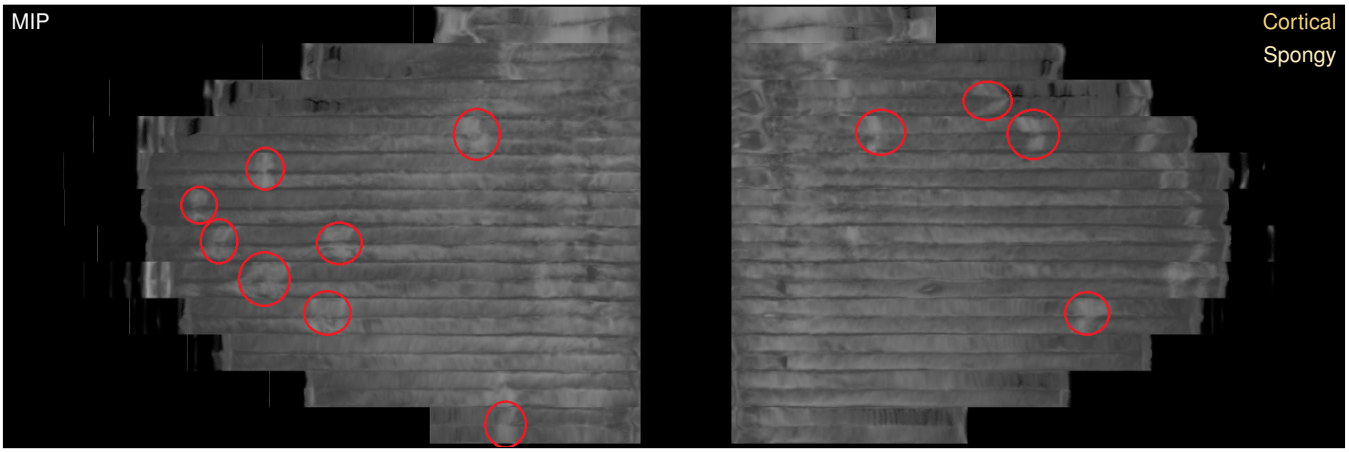

(a)

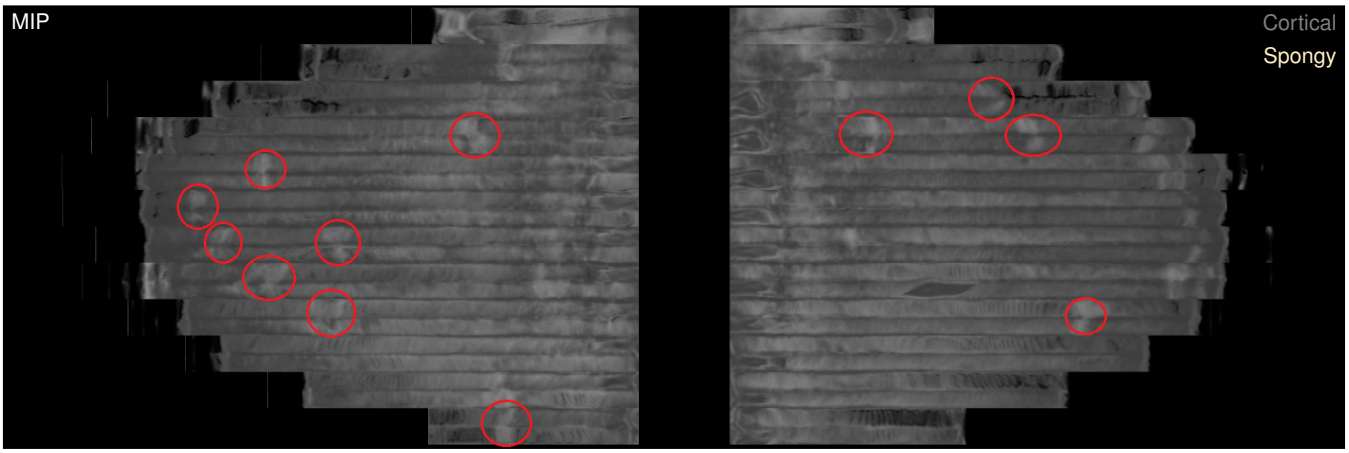

(b)

Figure 10: *Case with multiple osteoblastic rib bone metastases. (a) presents a MIP of both bone layers (cortical & spongy) that highlights the metastases with the surrounding cortical bone. (b) shows the same case, but with MIP considering the spongy layer only. Since the spongy bone layer exhibits lower intensity values than the cortical layer, the metastases are enhanced even stronger.*

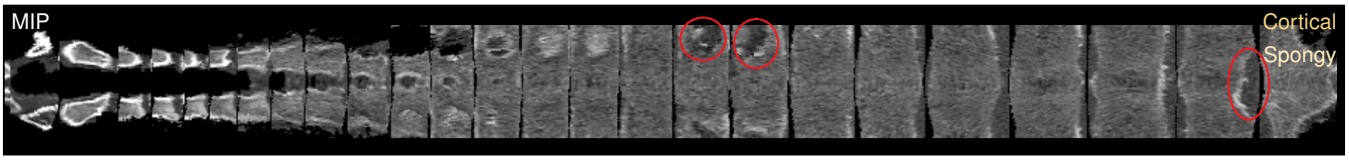

(a) Fractures

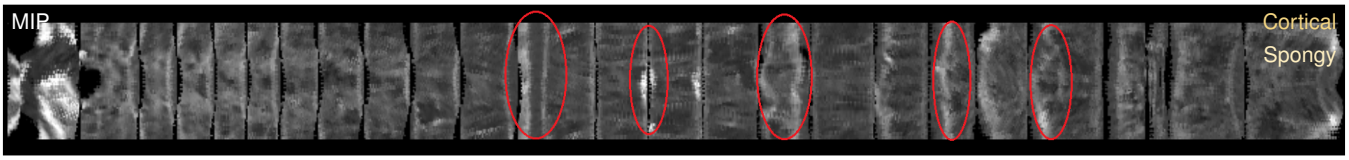

(b) Lesions

Figure 11: *Two cases with spinal bone fractures and metastases. (a) displays multiple fractures of different vertebrae using a MIP of both bone layers (cortical & spongy). (b) shows several lesions, again using a MIP of both bone layers (cortical & spongy).*

References

[AMB*13] AUZINGER* T., MISTELBAUER* G., BACLIJA I., SCHERNTHANER R., KÖCHL A., WIMMER M., GRÖLLER M. E., BRUCKNER S.: Vessel visualization using curved surface reformation. *IEEE Trans Vis Comput Graph 19*, 12 (2013), 2858–2867. (*contributed equally). 2

[AMRB98] ACHENBACH S., MOSHAGE W., ROPERS D., BACHMANN K.: Curved multiplanar reconstructions for the evaluation of contrast-enhanced electron beam CT of the coronary arteries. *American Journal of Roentgenology 170*, 4 (1998), 895–899. 2

[BGP*11] BORKIN M. A., GAJOS K. Z., PETERS A., MITSOURAS D., MELCHIONNA S., RYBICKI F. J., FELDMAN C. L., PFISTER H.: Evaluation of artery visualizations for heart disease diagnosis. *IEEE Trans Vis Comput Graph 17*, 12 (2011), 2479–2488. 2

[BHL*14] BATTLE C. E., HUTCHINGS H., LOVETT S., BOUAMRA O., JONES S., SEN A., GAGG J., ROBINSON D., HARTFORD-BEYNON J., WILLIAMS J., EVANS A.: Predicting outcomes after blunt chest wall trauma: development and external validation of a new prognostic model. *Critical Care 18*, 3 (2014), R98. 2

[BHP06] BADE R., HAASE J., PREIM B.: Comparison of fundamental mesh smoothing algorithms for medical surface models. In *Proceedings of SimVis* (2006), pp. 289–304. 4

[BSO*15] BIER G., SCHABEL C., OTHMAN A., BONGERS M. N., SCHMEHL J., DITT H., NIKOLAOU K., BAMBERG F., NOTOHAMIPRODJO M.: Enhanced reading time efficiency by use of automatically unfolded CT rib reformations in acute trauma. *European Journal of Radiology 84*, 11 (2015), 2173–2180. 2

[Flo97] FLOATER M. S.: Parametrization and smooth approximation of surface triangulations. *Computer Aided Geometric Design 14*, 3 (1997), 231–250. 2

[GMC*06] GUISE T. A., MOHAMMAD K. S., CLINES G., STEBBINS E. G., WONG D. H., HIGGINS L. S., VESSELLA R., COREY E., PADALECKI S., SUVA L., CHIRGWIN J. M.: Basic mechanisms responsible for osteolytic and osteoblastic bone metastases. *Clinical Cancer Research 12*, 20 (2006), 6213s–6216s. 3

[Her09] HERMAN G. T.: *Fundamentals of Computerized Tomography: Image Reconstruction from Projections*, 2nd ed. Springer Publishing Company, Incorporated, 2009. 4

[HMD*15] HOMANN G., MUSTAFA D. F., DITT H., SPENGLER W., KOPP H.-G., NIKOLAOU K., HORGER M.: Improved detection of bone metastases from lung cancer in the thoracic cage using 5- and 1-mm axial images versus a new CT software generating rib unfolding images. *Academic Radiology 22*, 4 (2015), 505–512. 3

[KFW*02] KANITSAR A., FLEISCHMANN D., WEGENKITTL R., FELKEL P., GRÖLLER M. E.: CPR - curved planar reformation. In *Proceedings of IEEE Visualization* (2002), pp. 37–44. 1, 2

[KFWG06] KANITSAR A., FLEISCHMANN D., WEGENKITTL R., GRÖLLER M. E.: Diagnostic relevant visualization of vascular structures. In *Scientific Visualization: The Visual Extraction of Knowledge from Data*, Bonneau G.-P., Ertl T., Nielson G., (Eds.), Mathematics and Visualization. Springer Berlin Heidelberg, 2006, pp. 207–228. 1, 2

[KKW*14] KAFTAN J. N., KOPACZKA M., WIMMER A., PLATSCH G., DECLERCK J.: A rib-specific multimodal registration algorithm for fused unfolded rib visualization using pet/ct. In *Proceedings of SPIE Medical Imaging: Image Processing* (2014), vol. 9034, p. 90341C. 2

[KMU*12] KUMAR V., MG S., U K., KC S., TS A. K., HALLIKERI V. R.: The comprehensive analysis of traumatic rib fractures and their complications: A post mortem study. *Journal of Forensic Research* (2012). 2

[KST*14] KRETSCHMER J., SOZA G., TIETJEN C., SUEHLING M., PREIM B., STAMMINGER M.: ADR - Anatomy-Driven Reformation. *IEEE Trans Vis Comput Graph 20*, 12 (2014), 2496–2505. 2

[KW15] KRZESZINSKI J. Y., WAN Y.: New therapeutic targets for cancer bone metastasis. *Trends in Pharmacological Sciences 36*, 6 (2015), 360–373. 3

[May16] MAYFIELDCLINIC: Anatomy of the spine. MayfieldClinic, (Ed.). 4

[MK16] MARINO J., KAUFMAN A.: Planar visualization of treelike structures. *IEEE Trans Vis Comput Graph 22*, 1 (2016), 906–915. 2

[MMK*17] MIAO H., MISTELBAUER G., KARIMOV A., ALANSARY A., DAVIDSON A., LLOYD D. F. A., DAMODARAM M., STORY L., HUTTER J., HAJNAL J. V., RUTHERFORD M., PREIM B., KAINZ B., GRÖLLER M. E.: Placenta maps: In utero placental health assessment of the human fetus. *IEEE Trans Vis Comput Graph 23*, 6 (2017), 1612–1623. 2, 4

[MMV*13] MISTELBAUER G., MORAR A., VARCHOLA A., SCHERNTHANER R., BACLIJA I., KÖCHL A., KANITSAR A., BRUCKNER S., GRÖLLER M. E.: Vessel visualization using curvicircular feature aggregation. *Computer Graphics Forum 32*, 3 (2013), 231–240. 2, 4

[MS11] MACCAURO G., SPINELLI M. S.: Physiopathology of spinemetastasis. *Journal of Surgical Oncology* (2011). 3

[OL12] ORTIZ A., LIN S.-H.: *Osteolytic and Osteoblastic Bone Metastases: Two Extremes of the Same Spectrum?* Springer Berlin Heidelberg, Berlin, Heidelberg, 2012, pp. 225–233. 3

[PB14] PREIM B., BOTHA C.: *Visual Computing for Medicine*, 2nd ed. Morgan Kaufmann, 2014, ch. e14 – Projections and Reformations, pp. e1–e17. 5

[RBH*11] RITTER F., BOSKAMP T., HOMEYER A., LAUE H., SCHWIER M., LINK F., PEITGEN H. O.: Medical image analysis. *IEEE Pulse 2*, 6 (2011), 60–70. 6

[RLT*15] RINGL H., LAZAR M., TÖPKER M., WOITEK R., PROSCH H., ASENBAUM U., BALASSY C., TOTH D., WEBER M., HAJDU S., SOZA G., WIMMER A., MANG T.: The ribs unfolded – a CT visualization algorithm for fast detection of rib fractures: effect on sensitivity and specificity in trauma patients. *European Radiology 25*, 7 (2015), 1865–1874. 2, 3, 4

[RSS*10] RINGL H., SCHERNTHANER R. E., SCHUELLER G., BALASSY C., KIENZL D., BOTOSANEANU A., WEBER M., CZERNY C., HAJDU S., MANG T., HEROLD C. J., SCHIMA W.: The skull unfolded: A cranial CT visualization algorithm for fast and easy detection of skull fractures. *Radiology 255*, 2 (2010), 553–562. 2

[Sar06] SAROUL L.: *Surface Extraction and Flattening for Anatomical Visualization*. PhD thesis, Ecole Polytechnique Federale De Lausanne, 2006. 2

[SBS*13] SORGER J., BÜHLER K., SCHULZE F., LIU T., DICKSON B.: neuromap – interactive graph-visualization of the fruit fly's neural circuit. In *IEEE Symposium on Biological Data Visualization* (2013), pp. 73–80. 2

[SHS*13] SCHULZE C., HOPPE H., SCHWEITZER W., SCHWENDENER N., GRABHERR S., JACKOWSKI C.: Rib fractures at postmortem computed tomography (PMCT) validated against the autopsy. *Forensic Science International 233*, 1–3 (2013), 90–98. 2

[Sie16] SIEMENS H.: *syngo.via Frontier – Your open platform for transational research*. 2016. 6

[TBB*07] TERMEER M., BESCÓS J. O., BREEUWER M., VILANOVA A., GERRITSEN F., GRÖLLER E.: CoViCAD: Comprehensive visualization of coronary artery disease. *IEEE Trans Vis Comput Graph 13*, 6 (2007), 1632–1639. 2

[WLP*12] WU D., LIU D., PUSKAS Z., LU C., WIMMER A., TIETJEN C., SOZA G., ZHOU S. K.: A learning based deformable template matching method for automatic rib centerline extraction and labeling in ct images. In *Proceedings of IEEE Conference on Computer Vision and Pattern Recognition* (2012), pp. 980–987. 2

[YLO11] YANG K.-M., LYNCH M., O'DONNELL C.: "Buckle" rib fracture: An artifact following cardio-pulmonary resuscitation detected on postmortem CT. *Legal Medicine 13*, 5 (2011), 233–239. 2

[ZA94] ZIEGLER D. W., AGARWAL N. N.: The morbidity and mortality of rib fractures. *Journal of Trauma 37*, 6 (Dec 1994), 975–979. 2